High-Resolution Crystal Structures of Villin Headpiece and Mutants with Reduced F-Actin Binding Activity[†,‡]

Jianmin Meng, Didem Vardar,[§] Yeming Wang, Hwai-Chen Guo, James F. Head, and C. James McKnight*

Department of Physiology and Biophysics, Boston University School of Medicine, 715 Albany Street, Boston, Massachusetts 02118

Received May 9, 2005; Revised Manuscript Received July 8, 2005

ABSTRACT: Villin-type headpiece domains are approximately 70 amino acid modular motifs found at the C terminus of a variety of actin cytoskeleton-associated proteins. The headpiece domain of villin, a protein found in the actin bundles of the brush border epithelium, is of interest both as a compact F-actin binding domain and as a model folded protein. We have determined the high-resolution crystal structures of chicken villin headpiece (HP67) at 1.4 Å resolution as well as two mutants, R37A and W64Y, at 1.45 and 1.5 Å resolution, respectively. Replacement of R37 causes a 5-fold reduction in F-actin binding affinity in sedimentation assays. Replacement of W64 results in a much more drastic reduction in F-actin binding affinity without significant changes in headpiece structure or stability. The detailed comparison of these crystal structures with each other and to our previously determined NMR structures of HP67 and the 35-residue autonomously folding subdomain in villin headpiece, HP35, provides the details of the headpiece fold and further defines the F-actin binding site of villin-type headpiece domains.

Villin-type headpiece domains are compact motifs found exclusively at the extreme C termini of several families of proteins associated with the actin cytoskeleton. Most but not all headpiece domains specifically bind actin filaments (F-actin) (*1*). Headpiece domains are about 70 amino acids long and remain folded and functional when expressed alone or cleaved from the larger N-terminal "core" domains of their parent proteins. Headpiece sequences are unrelated to any other F-actin binding protein or any other sequence in the Genbank database but show high sequence similarity (∼35−40%) to other villin-type headpiece domains.

The headpiece domain of villin provides the second F-actin binding site essential for the actin bundling activity of villin (*2*). Villin is a major component of the actin bundles that support the microvilli of the brush border membrane of the absorptive epithelium lining the gut and in the proximal tube of the kidney (*3*). The exact role that villin plays in the microvilli is unclear because knockout mice missing villin have essentially normal microvilli (*4*). Villin has been suggested to be involved in cell plasticity, probably through the F-actin severing activity of villin's gelsolin-like core domain (*5*). Villin contains three phosphatidylinositol 4,5-bisphosphate (PIP_2)[1] binding sites, one of which has been localized to the headpiece domain (*6*). We have reported the NMR structure of the last 67 residues of villin headpiece (HP67) (*7*) as well as the NMR structure of the C-terminal 35 residues (HP35) (*8*), which has been used extensively as a model system for both computational and experimental approaches to protein folding (*9*−*17*).

The actin-binding activity of villin headpiece has been investigated by several labs using mutational analysis (*18*−*21*). The key residues involved in actin binding include K38, E39, K65, residues 70−73: KKEK, G74, L75, and F76. Several studies have shown that the last two residues of the KKEK motif (E72 and K73) contribute less (if at all) to F-actin binding (*19*, *20*). When mapped onto the NMR structure of HP67, all but two of the residues implicated in actin-binding cluster together on the surface, identifying the actin-binding site. The two residues that are not found on the surface (E39 and K70) appear to form a buried salt bridge that is conserved in the NMR structure of the headpiece domain of dematin, an erythrocyte protein with a core domain unrelated to villin (*22*). The importance of the buried salt bridge to actin binding is underscored by the observation that the HP35 subdomain that contains all of the implicated F-actin binding residues except for K38 and E39 does not bind F-actin in standard sedimentation assays (*1*, *7*, *21*). On

[†] This work supported by National Institutes of Health Grant GM62886 to C.J.M.

[‡] The three crystal structures reported here have been deposited in the RCSB protein database under the accession codes 1YU5 for HP67, 1YU7 for W64Y, and 1YU8 for R37A.

* To whom correspondence should be addressed. E-mail: cjmck@bu.edu. Telephone: (617) 638-4042. Fax: (617) 638-4041.

[§] Current address: Department of Pathology, Brigham and Women's Hospital, Harvard Medical School, NRB 652, 77 Louis Pasteur Ave., Boston, MA, 02115.

[1] Abbreviations: ATP, adenosine triphosphate; CD, circular dichroism; DTT, dithiothreitol; HP67, 67 amino acid polypeptide encoding residues 10−76 of villin headpiece (residues 760−826 of intact chicken villin); HPLC, high-performance liquid chromatography; MAD, multiwavelength anomalous dispersion; NMR, nuclear magnetic resonance; PAGE, polyacrylamide gel electrophoresis; PCR, polymerase chain reaction; PEG, poly(ethylene glycol); PIP_2, phosphatidylinositol 4,5-bisphosphate; NSLS, National Synchrotron Light Source; R37A, mutant of HP67 replacing arginine 37 with alanine; rms, root-mean-square; SAS, solvent-accessible surface area; SDS, sodium dodecyl sulfate; T_m, unfolding midpoint; TRIS, tris(hydroxymethylamino)methane; UV, ultraviolet; V-loop, variable length loop; W64A, mutant of HP67 replacing tryptophan 64 with alanine; W64Y, mutant of HP67 replacing residue tryptophan 64 with tyrosine.

10.1021/bi050850x CCC: $30.25
Published on Web 08/16/2005

the basis of the distribution of the known actin-binding residues on the surface of HP67 and the two other residues highly conserved among headpiece domains (W64 and R37), we proposed a three-part binding motif (*7*) for high-affinity binding by headpiece domains to F-actin. This motif consists of a hydrophobic "cap", consisting primarily of the completely conserved W64, above a "crown" of alternating positive and negative charges, and a charged "patch" composed of K38 and K73 (see Figure 3).

Recently, Vermeulen et al. have examined the effect of a mutation of the hydrophobic cap residue W64 on actin binding (*21*). The mutation was made in the background of the 35-residue HP35 subdomain of human villin headpiece. They showed decreased binding with the W64A mutation relative to the wild type. However, these experiments are complicated by the very low affinity of the short HP35 constructs for actin. Indeed, cross-linking reagents were required to demonstrate binding even for the wild-type sequence.

Here, we report the high-resolution structure of HP67 at 1.4 Å resolution and compare it with our earlier NMR structure. The structure provides the exact details of the packing of the hydrophobic core, including the aromatic cluster that stabilizes the HP35 subdomain (*23*). The buried salt bridge that connects the N- and C-terminal halves of villin headpiece is unambiguous in the crystal structure, which also provides its exact geometry. In conjunction with our previous NMR data, the crystal structure also provides new insight into the dynamic nature of the variable length loop (V-loop) found in the N-terminal region of headpiece domains. Finally, examination of the F-actin binding surface in the crystal structure is consistent with our three-part binding motif model for F-actin binding but also indicates that the properties of the surface can vary significantly.

In conjunction with the high-resolution structure of HP67, we have also tested the role of the conserved residues W64 and R37 on actin affinity. We have used full-length headpiece domains and standard sedimentation assays. We find that even conservative replacement of W64 with tyrosine results in a dramatic loss of F-actin affinity while replacement with alanine causes a complete loss of specific binding. Replacement of R37 decreased but does not eliminate specific F-actin binding. We can directly assess the effect of these mutations on the structure and actin-binding surface of villin headpiece as we report the high-resolution crystal structures of two of the mutants, W64Y (1.5 Å resolution) and R37A (1.45 Å resolution) as well as their relative thermostabilities determined by thermal unfolding experiments monitored by circular dichroism (CD) spectroscopy.

EXPERIMENTAL PROCEDURES

Cloning, Expression, and Purification of Proteins. The pET24a-based expression vector pVHP10-76 (*7*) was used to express HP67. It encodes the last 67 residues of villin headpiece (HP67) corresponding to residues 760−826 of chicken villin. The two mutants, W64Y and R37A, were created by QuikChange mutagenesis using the instructions of the manufacturer (Stratagene). The W64A mutant was constructed from pVHP10-76 by PCR using mutagenic primers. The 5′ primer contained an *Nde* I restriction site and added an additional tyrosine codon right after the methionine initiation codon, and the 3′ primer contained an *Eco*R I restriction site and an alanine codon that replaced the tryptophan codon for residue 64. The additional tyrosine residue was incorporated at the N terminus of W64A to allow concentration determination of the mutant by UV absorbance as described below. The PCR product and expression vector pET24a (Novagen) were double-digested with *Nde* I and *Eco*R I, annealed, and ligated to produce the W64A expression vector (*33*). All mutations were confirmed by DNA sequencing (Boston University Medical Campus Genetics Core Facility).

All of the constructs were expressed in *Escherichia coli* BL21(DE3) cells (Novagen) and purified as described in ref *7*. Briefly, after the cells were lysed and a 30 min centrifugation at 17000*g*, the supernatant was applied to a Sephadex G-50 column. The lyophilized fractions containing the desired peptides were further purified by reverse-phase HPLC on a C18 column eluted with an acetonitrile−water gradient with 0.1% trifluoroacetic acid. Purified proteins were stored as a lyophilized powder.

Actin was purified from chicken pectoral muscle using standard procedures (*24*) and stored at 4 °C. Actin was freshly dialyzed against G buffer [5 mM tris(hydroxymethylamino)methane (TRIS) at pH 8.26, 0.2 mM $CaCl_2$, 0.5 mM dithiothreitol (DTT), 0.2 mM ATP, and 0.1 mM NaN_3] for 2 days before sedimentation assays. The G-actin concentration was determined by absorbance at 290 nm using an extinction coefficient of 26 640 L M^{-1} cm^{-1}. The concentrations of headpiece mutants were determined by absorbance at 280 nm using extinction coefficients of 5690 L M^{-1} cm^{-1} (for HP67 and R37A) and 1280 L M^{-1} cm^{-1} (for W64Y and W64A), respectively (*25*). The concentration measurements for G-actin and headpiece proteins were taken after 1 h ultracentrifugation (100000*g*) at 4 °C immediately before the sedimentation assay.

CD Spectroscopy. CD spectra were acquired on an Aviv 62DS spectrometer. For far-UV wavelength scans, samples were 20 μM protein in 10 mM sodium phosphate buffer at pH 7.0. An additional 100 mM NaCl was included for thermal unfolding experiments. For near-UV CD spectra, samples contained 200 μM peptide in 10 mM phosphate buffer at pH 7.0. Far-UV CD scans were collected at 1 nm intervals from 250 to 190 nm at 25 °C as the average of five scans with a 5 s integration time, in a 2 mm path-length cell. Near-UV CD scans were collected at 0.5 nm intervals from 310 to 250 nm at 25 °C as the average of five scans with a 5 s integration time in a 10 mm path-length cell. A spectrum of buffer alone was subtracted from each scan to correct for the baseline signal. For thermal unfolding experiments, the protein concentrations were 20 μM and data points were collected at 222 nm, with 25 s of signal averaging at 1 °C intervals from 20 to 100 °C after a 60 s temperature equilibration time in a 2 mm path-length cell.

Crystallization of HP67 and Mutant Headpiece Domains. Initial crystallization conditions were identified with a sparse matrix crystal screen (Crystal Screen, Hampton Research, Laguna Niguel, CA). Hanging droplets consisting of 1 μL of protein stock solution (30 mg/mL in pure water) mixed with 1 μL of the reservoir solution were equilibrated against 0.5 mL of reservoir solution. High salt conditions, 1.5 M Na and K phosphate buffer, and 100 mM 2-(4-(2-hydroxyethyl)-1-piperazinyl)ethanesulfonic acid at pH 7.0 were used

Table 1: Data Collection Statistics for HP67 Bromine Derivative

X-ray source	synchrotron		
space group	$P2_12_12_1$		
cell axes (Å)	31.2, 37.7, 52.9		
cell angles	90, 90, 90		
dataset	Br edge	Br max	Br remote
wavelength	0.9206	0.9202	0.9050
resolution range (Å)	100−1.75	100−1.75	100−1.72
redundancy (total/unique)	37.1 (250869/6769)	37.0 (250223/6767)	37.0 (261665/7070)
R_{sym}[a] (%), overall (final shell)	3.1 (6.9)	3.8 (8.0)	3.4 (7.4)
completeness (%), overall (final shell)	99.5 (97.9)	99.6 (98.8)	99.6 (99.3)
I/σ_I, overall (final shell)	32.3 (20)	31.3 (21)	31.7 (21)

[a] $R_{sym} = \sum_h\sum_i|I_{hi} - I_h|/\sum_h\sum_i I_{hi}$ for the intensity (I) of i observations of reflection h.

to crystallize HP67. For crystals of the W64Y and R37A mutants, 0.2 M ammonium sulfate, 0.1 M sodium cacodylate (pH 6.5), and 30% poly(ethylene glycol) (PEG) 8000 was used and the volumes of reservoir and protein stock solutions in the drops were doubled. Crystallizations were optimized by microseeding with a reduced protein stock concentration (15 mg/mL) and with an additional reduced precipitant concentration (25% PEG 8000) for the mutants. Crystals suitable for data collection (see Table 1) grew within 3 days at room temperature to ~300 μm maximum dimension.

HP67 crystals were cryoprotected by soaking sequentially in reservoir solutions containing 10 and then 20% ethylene glycol for 3 min. Crystals of the two mutants were cryoprotected by soaking sequentially in reservoir solutions containing 10% glycerol followed by 20% glycerol for 3 min. The crystals were then immediately frozen under N_2 vapor at 95 K. Diffraction data for HP67 were collected at the National Synchrotron Light Source (NSLS) beamline X8C Brookhaven, NY, and diffraction data for W64Y and R37A were collected on an RAXIS IV (Boston University School of Medicine). The data were processed with the HKL suite (HKL Research, Inc.).

The phases used to solve the HP67 structure were obtained by the multiwavelength anomalous dispersion method (MAD) of crystals soaked in NaBr (*26*). A crystal of HP67 was transferred to 20% PEG 4000 and 10 mM sodium cacodylate at pH 7.0 and soaked for 1 h. This crystal was then transferred briefly to a solution containing 20% PEG 4000, 10 mM sodium cacodylate at pH 7.0, 0.5 M NaBr, and 15% ethylene glycol. After 20 s in this solution, the crystal was frozen in the nitrogen stream (100 K) at the beamline. The crystal diffracted to better than 1.7 Å in space group $P2_12_12_1$ ($a = 31.2$ Å, $b = 38.1$ Å, and $c = 52.7$ Å). MAD data sets were collected for phasing from bound bromine atoms (Table 1). Six bromide sites were identified per asymmetric unit using SOLVE (*27*). Density modification was performed using RESOLVE (*28*), which also automatically built a polyalanine model for 37 residues. Density-modified maps showed readily identifiable density, and the remainder of the model was built using O (*29*). Rounds of refinement of the bromine-phased model and rebuilding were performed using CNS (*30*) and O. The refined bromine-phased model was then used as the starting model for structure determination of HP67, W64Y, and R37A by molecular replacement. Electron-density maps were calculated at 1.4, 1.5, and 1.45 Å for HP67, W64Y, and R37A, respectively. The structures were modeled using O and refined using torsional dynamics and the maximum likelihood target function in CNS. See Table 2 for structural statistics. The coordinates have been deposited in the RCSB protein database under the accession codes 1YU5 for HP67, 1YU7 for W64Y, and 1YU8 for R37A.

Actin Sedimentation Assay. Sedimentation assays were performed at 4 °C as described previously (*1*, *31*). The total reaction volume was 50 μL. G-actin (20 μM) was first incubated in F-buffer (10 mM TRIS at pH 8.0, 1 mM $MgCl_2$, 100 mM NaCl, 0.1 mM ATP, 0.2 mM DTT, 3 mM NaN_3, and 0.1 mM $CaCl_2$) for 1 h to allow polymerization to occur. Headpiece constructs (5−200 μM) were then added, and after 1 h incubation, the samples were centrifuged for 1 h at 100000*g* in a prechilled rotor at 4 °C. Supernatants (about 48 μL) were separated from pellets right after centrifugation. Then, 12 μL of 5× loading buffer [50 mM TRIS at pH 7.5, 2% sodium dodecyl sulfate (SDS), and 12% glycerol] was added to the supernatant. The pellets were washed once with F-buffer and then soaked in 12 μL of 5× loading buffer for 1 h at room temperature. F-buffer (46 μL) was added to the pellets to bring the final volume to 60 μL. β-Mercaptoethanol was added to each tube to a final concentration of 5% as a reducing agent. The samples were stored at −20 °C.

The supernatants and pellets were analyzed on 16.5% SDS−PAGE tricine gels (*32*), separately. Headpiece protein standards (2.5−30 μM) were included on the same gel as the pellets to determine the concentration of bound proteins. After electrophoresis, the gels were fixed in 0.5% glutaraldehyde for 20 min, incubated in 12% trichloroacetic acid for 1 h, and then stained in Coomassie brilliant blue (CCB-G 250) colloidal solution (*33*) for 12−16 h. The gels were briefly washed in 25% methanol solution (~5 min) and preserved in 20% ammonium sulfate solution until quantitation. Each experiment was repeated at least 3 times.

Quantitation was performed on a Bio-Rad GS-700 Imaging Densitometer, using Molecular Analysts software. Concentrations of bound headpiece proteins were determined from the headpiece standards on the same gel. Total headpiece concentrations (HP_{total}) were used as independent variables, and bound headpiece concentrations (HP_{bound}) were used as dependent variables during fitting. The final data points used in fitting were the average of three separate sedimentation experiments. The binding data were fit with Origin 6.0 (Microcal Software, Inc., Northampton, MA) as previously described (*1*). Three parameters, the equilibrium dissociation constant (K_D), maximal binding constant (B_{max}), and the nonspecific binding (NS) were obtained from the fitting. The fitting function (eq 1) was developed from the formalisms of ligand−receptor interactions described by Swillens (*34*)

$$[HP_{bound}] = \frac{B_{max}([HP_{total}] - [HP_{bound}])}{K_D + ([HP_{total}] - [HP_{bound}])} + NS([HP_{total}] - [HP_{bound}]) \quad (1)$$

Under the tested concentration range (5−200 μM), W64Y and W64A did not show saturable F-actin binding and fits to eq 1 were poor. Fixed values for B_{max} (22 μM) and NS

Table 2: Statistics of Data Collection and Processing

	HP67	W64Y	R37A
X-ray source	NSLS X8C	Raxis IV	Raxis IV
space group	$P2_12_12_1$	$P2_12_12_1$	$P2_12_12_1$
cell axes (Å)	31.22, 38.03, 52.71	31.42, 38.26, 52.81	31.38, 37.54, 53.53
resolution range (Å)	100−1.4	100−1.5	100−1.45
redundancy (total/unique)	20.1 (261357/12968)	6.2 (61575/9864)	4.2 (48531/11690)
R_{sym}[a] (%), overall (final shell)	5.3 (28.8)	6.1 (8.8)	5.4 (13.6)
completeness (%), overall (final shell)	99.6 (100)	92.3 (86.8)	99.2 (96.2)
I/σ_I, overall (final shell)	19.2 (7.6)	28.2 (17.2)	24.4 (8.8)
statistics of model refinement			
nonhydrogen atoms			
protein	537	512	508
water	95	93	92
R_{cryst}[b] (%)	19.2	19.2	19.2
R_{free}[c] (%)	21.6	21.0	21.1
rms deviations[d]			
bond length (Å)	0.009	0.008	0.009
bond angles (deg)	1.33	1.39	1.33
averaged B values (Å^2)			
main chain	13.5	10.3	13.0
side chain	15.9	12.9	14.9
water	24.4	21.9	23.7
Ramachandran plot (%)			
most favored	96.6	98.2	96.4
additional	3.4	1.8	3.6
disallowed	0	0	0

[a] $R_{sym} = \sum_h\sum_i|I_{hi} - I_h|/\sum_h\sum_i I_{hi}$ for the intensity (I) of i observations of reflection h. [b] $R_{crys} = \sum|F_{obs} - F_{calc}|/\sum|F_{obs}|$, where F_{obs} and F_{calc} are the observed and calculated structure factor amplitudes, respectively. [c] R_{free} was calculated as R_{cryst} but with 8% of the amplitudes chosen randomly and omitted from the start of refinement. [d] rms deviations are deviations from ideal geometry.

(1.0%) were used when fitting W64Y. A pure linear model (eq 2) corresponding to nonspecific binding only was used to fit the W64A binding data

$$[HP_{bound}] = NS[HP_{total}] + A \quad (2)$$

where A represents any constant offset in the y axis.

RESULTS

Comparison of the HP67 Crystal and NMR Structures. The crystal structure of HP67 (Figure 1) is in overall agreement with its solution NMR structure (*7*). The root-mean-square (rms) deviation of the backbone heavy atoms between the crystal structure and the minimized average NMR structure is 1.7 Å, omitting the first three residues that are not ordered in the NMR structure and have weaker electron density in the HP67 crystal structure (Figure 2a). While the difference in conformation is distributed throughout the structures, the conformation of the V-loop (residues 21−29) is significantly altered and the turn between the two C-terminal helices packs closer to the core in the crystal structure altering the angle of those helices with respect to the rest of the molecule.

Because the C-terminal 35 residues of HP67 folds to form a thermostable subdomain independent of the N-terminal domain (*35*), we consider the structure to be composed of an N-terminal subdomain (residues 9−41) and a C-terminal subdomain (residues 42−76). However, inspection of the HP67 structure does not suggest that there are two subdomains because they appear to share a single hydrophobic core. Figure 1c shows the residues within the hydrophobic core, which we define as all residues with 20% or less solvent-accessible surface area (SAS). The solvent accessibilities of the individual residues in the crystal and NMR structures are similar. The largest change is in residue D28 that has 17% SAS in the previous NMR structure and 43% SAS in this crystal structure. In the crystal, D28 forms an intermolecular salt bridge to the amino terminus of a lattice mate that may account for part of this difference in SAS.

In the crystal structure, the N-terminal domain contains little regular secondary structure. Residues L18−V22 form a short α helix, and there are two 3−10 helices, A26−D28 and K38−H41. Although the two 3−10 helices were not identified in any of the ensemble of 10 NMR structures, the minimized average structure (PDB 1QQV) does have a 3−10 helix between residues E39−H41. The other 3−10 helix in the crystal structure, between residues A26−D28, falls within the V-loop region where in the NMR structure there is a type-I β turn between residues V22−D28. This change in conformation could be in part due to the salt bridge formed between the side chain of D28 and the amino terminus of a lattice mate. The V-loop region in the crystal structure also has higher B factors than all but the five N-terminal residues.

In the C-terminal subdomain, the crystal structure is more similar to that of the NMR structure than the N-terminal subdomain. The rms deviation of backbone atoms for residues L42−F76 between the minimized average NMR structure and the crystal structure is 1.2 Å. There are three α-helical segments in the crystal structure spanning residues D44−F51, R55−N60, and L63−K73. These helical segments closely correspond to those seen in the NMR structure (D44−V50, R55−F58, and W64−K73), although they are 1−2 residues longer in the crystal structure.

The crystal structure also clearly shows the structural details of the geometry of the buried salt bridge between E39 in the N-terminal subdomain and K70 in the C-terminal subdomain (Figure 2a). This salt bridge was inferred from the NMR structure, but the lack of constraints on the charged

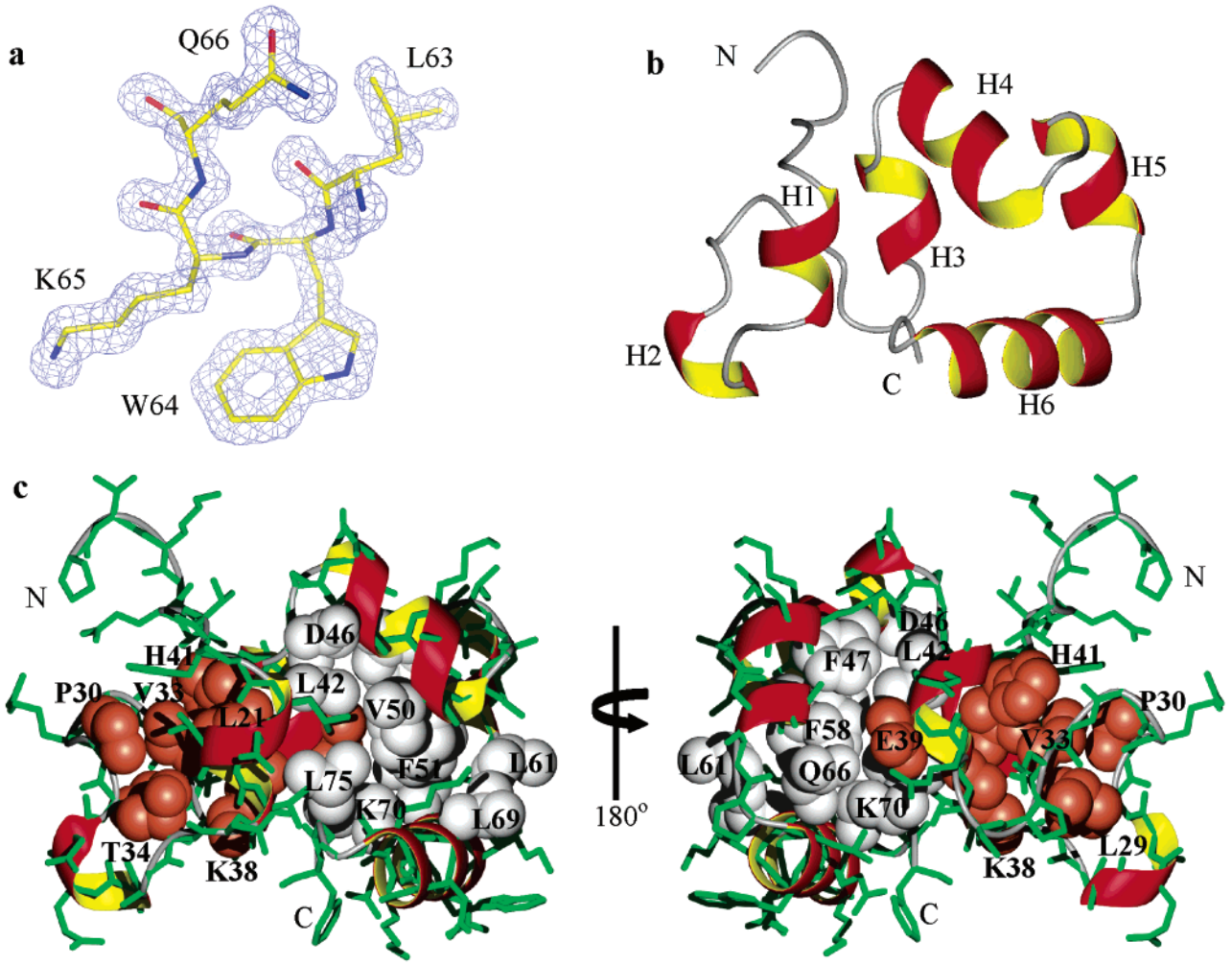

FIGURE 1: Crystal structure of villin headpiece, HP67. (a) Sample of the electron-density map for HP67 ($2F_o - F_c$, contour level 1.5, light blue) in the region near W64. Carbon bonds are shown in yellow; nitrogen is shown in dark blue; and oxygen is shown in red. (b) Ribbon representation of the backbone of HP67 with helices labeled 1−6. (c) Hydrophobic core of HP67. The side-chain heavy atoms of residues with 20% or less solvent-accessible surface area are shown as spheres and labeled. Core residues from the N-terminal subdomain (residues 10−41) are red, and those from the C-terminal subdomain (residues 42−76) are shown in white. All other side chains are shown as green sticks. The N and C termini are labeled. The view on the left is in an orientation similar to b, while the view on the right is rotated approximately 180° about the vertical axis.

side chain groups (that lack hydrogens) made it difficult to determine the exact geometry. The side chain of Glu 39 is in a different rotomer in the crystal structure than in the NMR structure (X-ray, $\chi_2 = -80°$ and $\chi_3 = 5°$; NMR, $\chi_2 = 110°$ and $\chi_3 = 105°$). The side-chain χ angles also differ in Lys 70, but both side chains are extended in roughly the same direction. The minimal distance between the carboxyl oxygen atoms of E39 and the side-chain nitrogen atom of K70 is reduced from 4.5 to 2.8 Å in the crystal structure compared with the NMR structure. In the crystal structure, water molecules are visible that hydrogen bond to the remaining ~10% of the accessible surface area of the charged side-chain functional groups of E39 and K70, stabilizing the buried polar interaction.

Of the 58 non-glycine or proline residues in the crystal structure, 97% (56 residues) of the backbone ψ and ϕ angles fall in the most favored region of Ramachandran map and the other 3% (2 residues) are in the additionally allowed region. This is in contrast to the minimized average NMR structure, where 77% (48 residues) are in the most favored region, 12% (7 residues) are in the additionally allowed region, and 6% (3 residues) are in the generously allowed region. The largest changes in ψ and ϕ angles between the two structures are for residues 11−12, 22−24, 31−32, 62−63, and 73−75. All of these residues correspond to regions between secondary structural elements.

Comparison with the Thermostable HP-35 Subdomain. The backbone rms deviation between the crystal structure and the NMR structure of 35-residue villin headpiece subdomain, HP35 (PDB 1VII), is 1.3 Å, excluding the three C-terminal residues that are disordered in solution (*8*, *36*). The C-terminal helix is the site of the greatest difference between the two structures. Using the backbone to align the structures, the side chains of the residues composing the hydrophobic core (L42, F47, F51, F58, Q66, K65, and L69) occupy essentially the same space in both structures (Figure 2b). The backbone ψ and ϕ angles are similar between the NMR and crystal structures except at residues G52 and M53 in the region connecting the N-terminal and central helices of the subdomain, resulting in a slight change in the orientation of the central helix.

F-Actin Binding Face of HP67. In our earlier work (*7*), we proposed the requirement for a three-part binding motif for micromolar F-actin affinity by mapping onto the HP67

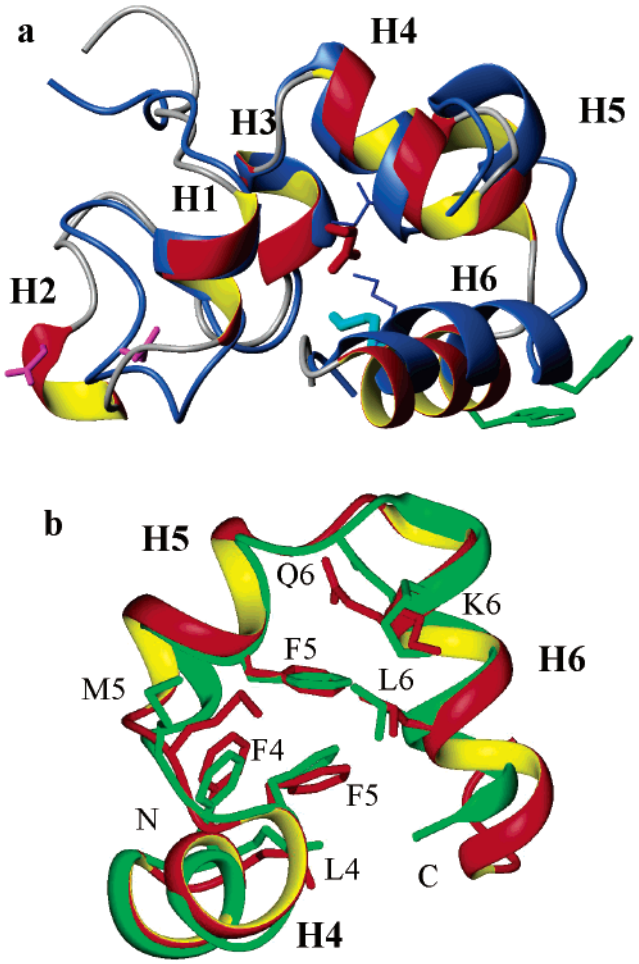

FIGURE 2: Comparison of the crystal structure of HP67 with the NMR structures of the HP67 and HP35 subdomains. (a) Overlay of the backbone ribbon diagrams of the crystal and NMR structures of HP67. The structures are fit to the backbone atoms of residues 14−20 and 30−52. The crystal structure is in red, yellow, and gray, and the NMR structure (PDB 1QQV) is in blue. The orientation is similar to that in Figure 1b. The side chains of E39 (red) and K70 (cyan) from the crystal structure that form the buried salt bridge are shown. To highlight the differences in the salt bridge between the crystal and NMR structures, the E39 and K70 side chains from the NMR structure are in blue. Also shown are the side chains of D28 (magenta) and W64 (green) to highlight the differences between the crystal and NMR structures. (b) C-Terminal region of the HP67 crystal structure corresponding to helices H4−H6 is shown in red and yellow, and the HP35 NMR structure (PDB 1VII) is in green. The NMR structure is overlaid on the backbone heavy atoms of residues 42−73 of the crystal structure. The side chains of residues L42, F47, F51, F58, Q66, K65, and L69 in the hydrophobic core from both structures are also shown and labeled. The side chain of M53 and the N and C termini are labeled.

NMR structure those residues biochemically implicated in F-actin binding (*18*, *19*) and surface residues conserved among headpiece domains. This motif consists of a "hydrophobic cap" dominated by the side-chain indole ring of W64 that sits above a "crown" of alternating positive and negative charges that wraps nearly around the entire molecule and a positively charged "patch" below the crown (Figure 3). A comparison of the surface of the crystal and NMR structures supports the major features of this model but also suggests some additional possibilities. The hydrophobic cap, composed from W64, which is the only residue completely conserved among all headpiece domains, is clear in both the

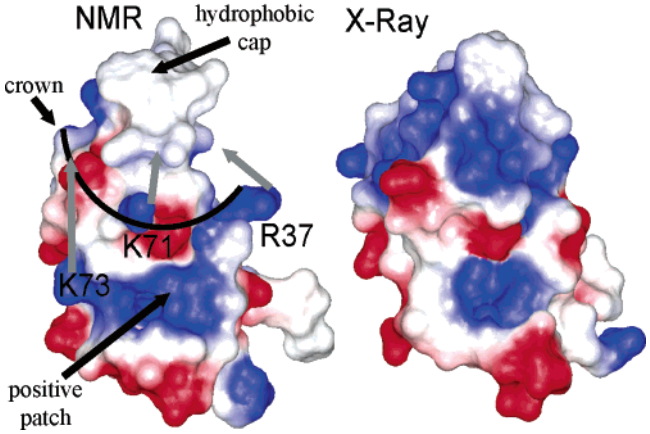

FIGURE 3: Comparison of the charged surface potential of the putative actin-binding faces of the HP67 NMR (left) and crystal (right) structures. Blue represents positive charge; red represents negative charge; and white is neutral. The residue number labels on the NMR structure indicate surface residues with large differences in conformation in the crystal and NMR structures. The gray arrows indicate the position of these residues in the crystal structure. The hydrophobic cap, charged crown, and positive patch features of the putative binding face are labeled on the NMR structure.

X-ray and NMR structures. Likewise, the positive patch feature is also visible in both the crystal and NMR structures.

The major difference in the putative actin-binding surface between the NMR and crystal structures is in the charged crown. The negative charges from the side-chain carboxyl of E72 and the C-terminal carboxyl group (from F76, the last residue of villin) are in similar positions in both structures. However, in the crystal structure, the long, positively charged side chains of R37, K71, and K73 all move toward the hydrophobic cap relative to the NMR structure (3.8, 4.4, and 9.7 Å, respectively). The positions of the atoms in these surface residues in the NMR structure are not tightly fixed, and examination of the 10 accepted structures shows that for R37 and K71 some of the structures have their side chains in close proximity to those of the crystal structure. However, for the side chain of K73 in the ensemble of NMR structures, the conformation is still over 5 Å from that in the crystal structure. At least part of this large change in side-chain location may be accounted for by intermolecular hydrogen bonding between lattice mates in the crystal structure. The side chain of K73 forms an intermolecular salt bridge to the side-chain carboxyl group of D19 of a neighboring lattice mate. Likewise, in the crystal structure, the side chain of R37 forms an intermolecular hydrogen bond to the backbone carbonyl of P10 and the side chain of K71 forms an intramolecular hydrogen bond to the side chain of N68. The changes in position of these positively charged residues are shown with arrows on the NMR structure in Figure 3.

Design, Structure, and Stability of HP67 Actin-Binding Mutants. Two residues, W64, which is invariant in all headpiece sequences, and R37, which is a conserved, positively charged residue in most sequences, are found on the putative actin-binding face of HP67. We have previously proposed that these residues contribute to F-actin binding (*7*). Vermeulen et al. have recently demonstrated the importance of W64 in the context of the C-terminal 35-residue subdomain from human villin headpiece by comparing the wild-type sequence with the W64A mutant using a

chemical cross-linking assay to overcome the very low actin affinity of their constructs (*21*). To test the role of W64 in the context of a full-length, high-affinity headpiece domain, we made two point mutants in HP67 that replace W64. While the first mutant, W64A, as in the previous study, completely removes the aromatic side chain, the second mutant, W64Y, is more conservative and thus results in a smaller yet still aromatic and hydrophobic side chain at position 64. We also tested the role of the conserved positive charge at position 37 by constructing a point mutant of HP67 that replaces the arginine side chain with alanine (R37A). The actin-binding activity of these three mutants was then quantitated and compared with HP67 using sedimentation assays; their thermostabilities were determined by thermal unfolding monitored by CD; and the structures of the W64Y and R37A mutants were determined by X-ray crystallography.

CD spectra in the far UV region (Figure 4a) indicate that all three mutants have secondary structure contents similar to HP67 in solution. The two mutants that replace tryptophan have slightly less intensity at 222 nm, suggesting a significant contribution of the indole ring to the CD signal of HP67. The close correspondence of the crystal structures of W64Y and HP67 (see below) coupled with the similarity of their fingerprint regions in two-dimensional NOESY NMR spectra (not shown) indicate that the lower CD signal at 222 is not due to changes in the structure.

Near-UV CD spectra are sensitive to aromatic residues and report on the tertiary structure. In the near-UV CD, R37A is almost identical to HP67 (Figure 4b). Similar to HP67 and R37A, negative bands are observed at 255, 262, and 268 nm for W64Y and W64A. However, the large, broad negative intensity contribution of the indole ring is missing for W64A. A broad positive component in the near-UV CD spectrum of W64Y likely arises from the contribution of the tyrosine side chain.

To test the effect of these mutations on the thermostability of HP67, we monitored the CD signal at 222 nm as a function of the temperature (Figure 4c). HP67 is thermostable with a thermal unfolding midpoint (T_m) of 77 °C at pH 7.0 (*1*). The T_m of R37A is essentially identical to that of HP67. Both W64A and W64Y have only a 6 °C decrease in their T_m values (71 °C) and are fully folded at all temperatures below 50 °C. Thus, the mutants retain the high thermal stability of HP67, indicating that they are fully folded and retain the native structure of HP67.

Crystal Structures of HP67 Mutants. To ensure that the mutations at positions 64 and 37 do not affect the global structure of HP67 but solely the putative F-actin binding face, we determined the crystal structures of the W64Y and R37A mutants to 1.50 and 1.45 Å, respectively. The crystal structures are essentially identical to that of HP67 except in the region around the mutation (Figure 5). The backbone rms deviation between the W64Y mutant and the HP67 structure is 0.3 Å, and the all atom rms deviation is 0.6 Å, excluding the mutated residue 64. For R37A, the backbone rms deviation is 0.2 Å and the all atom rms deviation, excluding the mutated residue 37, is 0.6 Å. Even the mutated side chains of W64Y and R37A overlay extremely close with their respective side chains in the HP67 structure (parts b and c of Figure 5). Thus, these mutations have essentially no effect on the three-dimensional structure of villin headpiece.

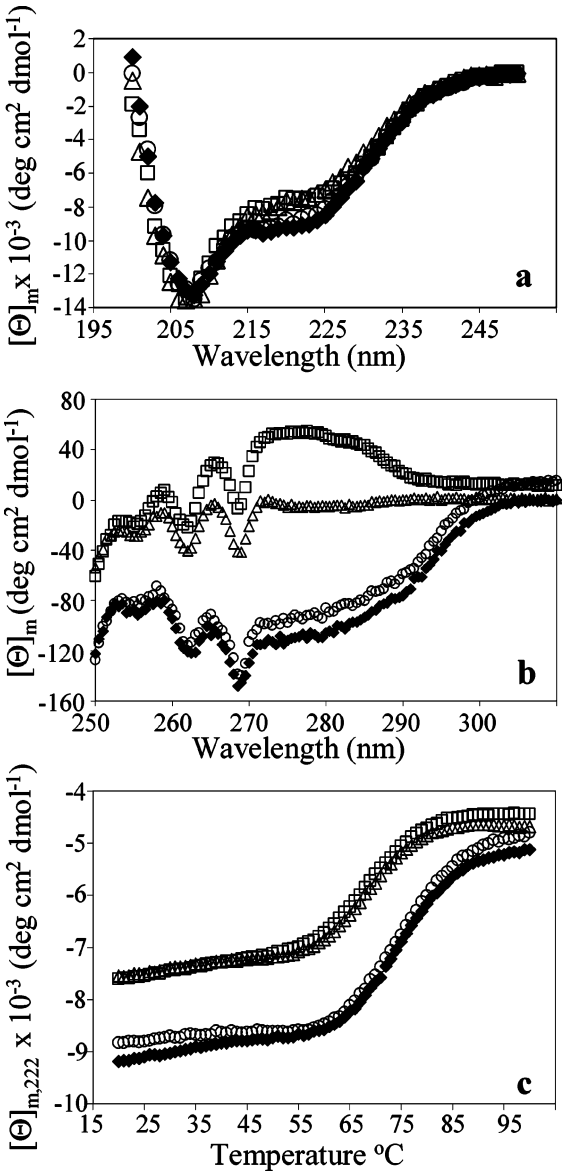

FIGURE 4: CD spectra and thermal unfolding of HP67 actin-binding mutants. (a) Far-UV scans of 20 μM protein at 25 °C in 10 mM sodium phosphate buffer at pH 7.0 in a 2 mm path-length cell. (b) Near-UV spectra of 200 μM peptide at 25 °C in 10 mM phosphate buffer at pH 7.0 in a 10 mm path-length cell. (c) Thermal unfolding of 20 μM protein in 10 mM phosphate with 100 mM NaCl at pH 7.0, monitored at 222 nm in a 2 mm path-length cell. HP67 (◆), R37A (○), W64Y (□), and W64A (△).

Actin Binding by HP67 Mutants. To test the effect of the mutations at position 64 and 37 of HP67 on F-actin affinity, we determined the binding constants for the three mutants using sedimentation assays. In this assay, increasing concentrations of the headpiece domain of interest are incubated with F-actin followed by high-speed centrifugation that sediments the large F-actin filaments. Proteins bound to F-actin cosediment with the filaments and are found in the pellet fractions, while unbound protein remains in the supernatant. The pellets and supernatants are separated and run on a SDS−PAGE gel, and the amounts of protein in the supernatant and pellet are quantitated. The K_D and maximum amount of protein specifically bound (B_{max}) are determined by fitting the binding curve as described in the Experimental Procedures. Because the binding constants for headpiece domains are relatively high (i.e., in the low micromolar range),

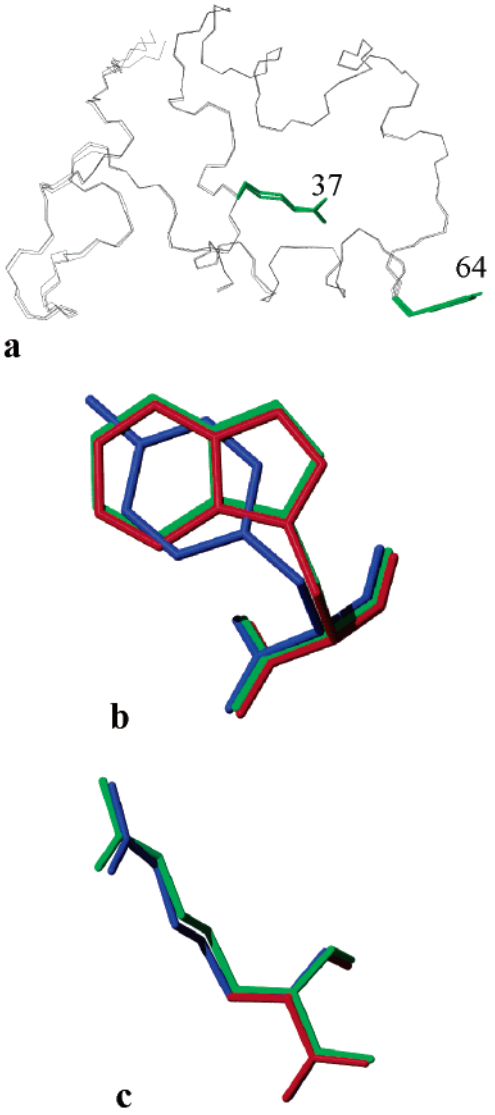

FIGURE 5: Comparison of mutant and wild-type HP67 crystal structures. (a) Backbone trace of the crystal structures of HP67, H41Y, and R37A. The side chains of W64 and R37 are shown in green. The view is similar to that in Figure 1b. In b and c, the sites of the mutation are highlighted in the superimposed crystal structures of HP67 (green), W64Y (blue), and R37A (red) in the region of (b) W64 and (c) R37. The backbone heavy atoms of residues 13−76 of the mutants were fit to those of the wild-type HP67 crystal structure.

high protein concentrations (up to 200 μM) are necessary, which can result in appreciable nonspecific binding (NS).

Figure 6a shows representative sedimentation experiments for HP67 and the three mutants. Plots of the average binding data and curve fits are shown in Figure 6b, and the K_D, B_{max}, and NS values are presented in Table 3. The K_D value of 4.1 ± 0.5 μM for HP67 is in good agreement with previously measured values (*1*, *31*). The B_{max} value is consistent with 1:1 headpiece/F-actin monomer binding. For R37A, the K_D value is reduced over 5-fold (24 ± 5.7 μM), while the B_{max} value is comparable to HP67. The reduced K_D value for R37A indicates that, while R37 has a significant contribution to the affinity of HP67 for F-actin, it is not essential for specific binding.

The results of the sedimentation experiments for W64A and W64Y are dramatically different from those of HP67

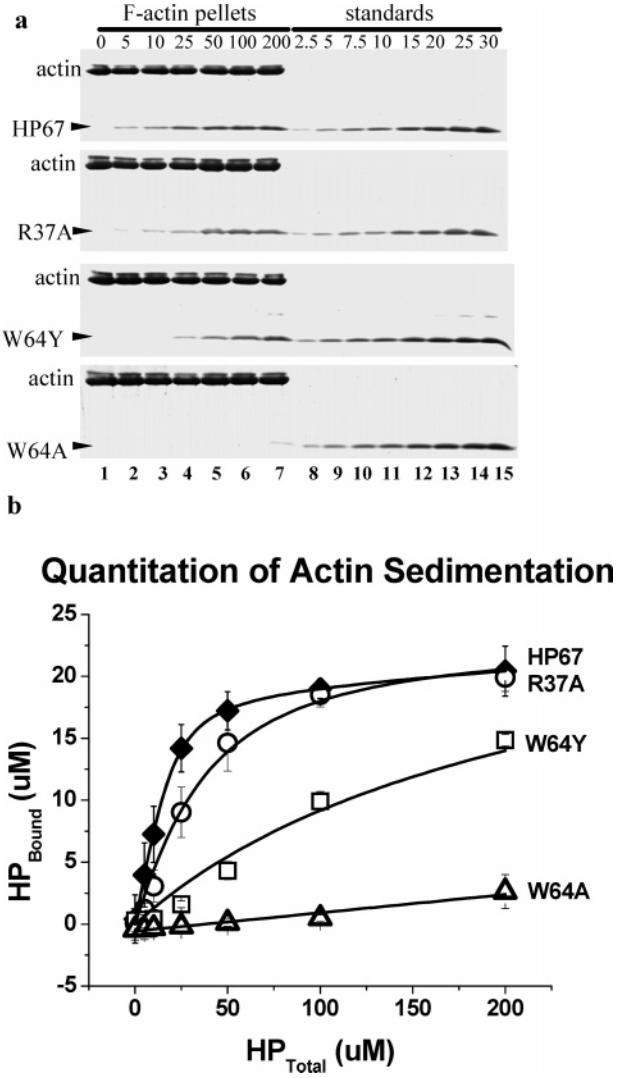

FIGURE 6: F-actin sedimentation assay. (a) Representative gels of the sedimentation assay. Lanes 1−7, 20 μM F-actin was incubated with the concentration of the headpiece domain indicated above each lane for 1 h at 4 °C before sedimentation at 100000*g* for 1 h. After removal of the supernatant, the pellet fractions containing bound proteins were separated on the gel and stained with Coomasie blue as described in the text. Lanes 8−15 are peptide standards run to aid in quantifying the amount of protein cosedimenting with F-actin. The concentrations of the headpiece domain loaded are indicated above each lane. The bands corresponding to actin and the respective headpiece domains are labeled. (b) Quantitation of the F-actin sedimentation assay. The concentration of the headpiece domains cosedimenting with F-actin are plotted against the total headpiece concentration in each reaction. The data points are the average of three separate experiments, and the error bars indicate the standard deviations of the three experiments. The curves are the best fit to the average data points. For HP67 and R37A, a saturation binding equation that includes nonspecific binding was used (see the text for details). For W64Y, the curve is the fit with a fixed B_{max} (22 μM), NS (1%), and K_D of 151 μM. For W64A, a linear fitting corresponding to nonspecific binding only is shown. HP67 (◆), R37A (○), W64Y (□), and W64A (△).

or R37A. Neither binding curve fits well to the equation for specific binding. Both mutants accumulate protein in the pellets in an essentially linear fashion without displaying any saturation. For W64A, the binding is consistent with nonspecific binding of 1.5%, which is comparable to nonspecific binding of HP67 (1%). For W64Y, there is significantly more

Table 3: HP67 and Mutant F-Actin Binding Parameters[a]

construct	K_D (μM)	B_{max} (μM)	NS (%)
HP67	4.1 ± 0.5	19 ± 0.5	1.0 ± 0.3
R37A	24 ± 5.7	23 ± 1.6	0.0 ± 0.3
W64Y	n/a[b]	n/a[b]	7.8 ± 0.6
W64A	n/a[b]	n/a[b]	1.5 ± 0.1

[a] Binding parameters (K_D, B_{max}, and NS) were determined by fitting the average values from three sedimentation experiments as described in the Experimental Procedures. [b] The binding W64Y and W64A did not display saturation and gave poor fits; therefore, a linear fit corresponding to nonspecific binding only is reported here.

peptide bound, suggesting either higher nonspecific binding because of the presence of the tyrosine residue or more likely a weak component of specific binding. To estimate the K_D for W64Y, we fixed the B_{max} and NS values and used eq 1 to fit only the K_D. Using a B_{max} value of 22 μM (the average of the other two peptides to require 1:1 binding for W64Y) and setting the nonspecific binding to 1% (the average value of the other three peptides), the calculated K_D for W64Y is 150 ± 17 μM, although the fit is poor. This K_D value is probably a lower limit on the true K_D of W64Y. The greatly reduced binding of both mutants lacking W64 demonstrates the critical role for tryptophan 64 in F-actin binding.

DISCUSSION

The villin headpiece domain is of interest both for its actin-binding activity and as a simplified model folded protein. Villin headpiece (and other villin-type headpiece domains) are independent binding motifs that fold to a thermostable structure without the aid of disulfide bonds, bound ligands, or oligomerization (*35*). In this paper, we present the very high-resolution (1.4 Å) crystal structure of villin headpiece (HP67). The structure provides a very precise view of the packing of the hydrophobic core. In particular, the buried salt bridge from residue E39 in the N-terminal subdomain to K70 in the C-terminal subdomain is clearly defined. This salt bridge is an important structural motif for actin-binding because mutation of either residue results in a significant decrease in actin binding (*19*). The salt bridge most likely assists in orienting and fixing the C-terminal residues that are important for F-actin binding, because the 35-residue subdomain that contains the C-terminal residues but lacks the salt bridge does not bind F-actin in sedimentation assays (*1*, *7*).

The crystal structure and the previously determined NMR structure are in good overall agreement. The crystal structure is somewhat more compact than NMR structure. This could be a result of tight packing within the crystal lattice. The limited distances observable by NOEs (i.e., <5 Å) may also contribute to the more extended conformation seen in the NMR structure. When the crystal and NMR structures are aligned on the backbone of the core of the structure (residues 14−20 and 30−52, backbone rms deviation of 1.05 Å), the turn between the two C-terminal helices is closer to the core in the crystal structure. The position of the C_α atom of W64 in the turn between the two C-terminal helices is shifted 5.4 Å closer to the core relative to its position in the NMR structure. There is also a change in the ψ angle of P62 (150° X-ray to −80° NMR) and ϕ angle of L63 (−54° X-ray to 168° NMR) in this turn region. These angles were not restrained in the NMR structure. The overall effect is that the turn region between the two C-terminal helices is pulled closer to the core in the crystal structure relative to the NMR structure. This also pulls the C-terminal end of helix 5 and the N-terminal end of helix 6 toward the core, while their distal ends are in a similar location in the crystal and NMR structures.

One of the most significant changes between the crystal and NMR structures is in the V-loop region. This region varies in length from 2 to 9 residues in the known headpiece sequences (*1*). In the crystal structure, residues 22−28 in the V-loop form a 3−10 helix in contrast to the NMR structure, where this same region forms a type-I β turn. Part of this difference in the V-loop secondary structure may be the result of an intermolecular salt bridge from the side-chain carboxyl of D28 to a lattice mate. However, the *B* factors in the V-loop region are higher than the rest of the structure (other than the N-terminal ~5 amino acids), suggesting more mobility in this loop. The higher mobility of the V-loop is consistent with the higher rms deviation in same region in the NMR structure. Also consistent are ^{15}N relaxation measurements in the headpiece domain of dematin that indicate that its V-loop is more mobile than the rest to the protein, in solution (*22*). Thus, it appears that the V-loop is dynamic and may sample multiple conformations.

Villin headpiece harbors an autonomously folding, monomeric subdomain of 35 residues (HP35) that has been used extensively as a model system for both experimental (*36*−*39*) and computational approaches to investigate protein folding (*9*−*17*). The C-terminal half of the crystal structure of HP67 is in good agreement with our previous NMR structure (*8*), with a backbone rms deviation of 1.3 Å, excluding the three C-terminal residues that are disordered in the subdomain in solution. The residues in the hydrophobic core occupy essentially the same volume in both the NMR and crystal structures (Figure 2b). In particular, the three phenylalanine residues that form an aromatic cluster in the core (*23*) are in nearly identical positions in the two structures. In this crystal structure, the side chain of methionine 53 packs closer to the hydrophobic core than in the HP35 NMR structure, further shielding the hydrophobic core residues F51, F58, and L69 from the solvent. The closer contact of the M53 side chain and the core is also consistent with the HP67 NMR structure, where NOEs were observed from the terminal methyl to the core residues. The terminal methyl of M53 was not assigned during the HP35 NMR structure determination, and therefore, no such restraints were included. Thus, it is likely that the M53 side chain in the HP35 subdomain also makes the closer contact with the hydrophobic core seen in this crystal structure.

Recently, the NMR structures of the C-terminal subdomains of human villin and limatin have also been reported (*21*). These structures are in agreement with the crystal structure of HP67 from chicken reported here as well as our previously determined NMR structures of HP67 and HP35. They all contain the characteristic three helices surrounding a hydrophobic core with an aromatic cluster of three phenylalanine residues (*23*). Because there were no minimized average structures deposited for these subdomains, we have used the conformer with the lowest rms deviation to the 25 reported structures for each to compare with the crystal structure. The rms deviation of the C-terminal region of the crystal structure, excluding the three C-terminal resi-

dues that may be unstructured in the subdomain constructs, is 1.75 Å for the human villin subdomain and 3.52 Å for the human advillin subdomain. Thus, the structures of the chicken and human villin C-terminal subdomains are more similar to each other than to that of advillin as would be expected on the basis of their higher primary sequence similarity.

The crystal structure of HP67 offers an additional view of the F-actin binding surface that compliments the previous NMR structure. This same surface is likely involved in PIP_2 binding because a peptide encompassing the residues in helix 6 has been shown to bind PIP_2 (*6*). In the crystal structure, interpretation of the surface of HP67 is somewhat complicated by the salt bridges and hydrogen bonds to other molecules in the crystal lattice, while in the NMR structure, the surface side chains are generally less well-fixed. Surface side chains may also change position upon interaction with F-actin. Nonetheless, the gross features of the binding face can be discerned and are consistent with our previous F-actin binding face hypothesis. In that hypothesis, the F-actin binding face consists of a tripartite motif consisting of (1) a hydrophobic cap composed mostly of W64, (2) a "crown" of positive and negative charges including R37, K65, K71, E72, K73, and the C-terminal carboxyl group of F75, and (3) a "positive patch" below the crown provided by residue K38. Some of the residues in the "charged crown" probably do not contribute significantly to binding; in particular, E72 and K73 have been shown to contribute minimally to actin binding (*19*, *20*). The hydrophobic cap and positive patch features are clear in both the crystal and NMR structures. The charged crown is altered, with three of the positively charged residues (R37, K17, and R73) extending their side chains up toward the hydrophobic cap in the crystal structure. It is important to note that these residues are all involved in intermolecular contacts with other molecules in the lattice, and those interactions are likely to affect their orientation. However, this does indicate that side chains of these residues are able to accommodate a range of positions upon F-actin binding.

To test the validity of the hydrophobic cap in actin binding, we examined the F-actin affinity of HP67 and two mutants that replace W64 either conservatively with tyrosine (W64Y) or, more substantially, with alanine (W64A). W64 is the only completely conserved residue in all known headpiece sequences. W64 has been implicated in F-actin binding in the context of the 35-residue subdomain of human villin by Vermeulen et al.; however, those constructs bind F-actin very weakly, and chemical cross-linking was required in that study to demonstrate binding, even for the wild-type peptide (*21*). In that study, replacement of the tryptophan residue with alanine resulted in a qualitative reduction in cross-linking to F-actin.

We have used a quantitative sedimentation assay to measure binding constants for full-length constructs that do not require chemical cross-linking. In our experiments, we use a constant amount of F-actin and increasing peptide concentrations to determine the binding constant, K_D, and the saturating concentration of peptide, B_{max}. For HP67, the K_D value is 4.1 ± 0.5 μM and the B_{max} value is 19 ± 0.5 μM. This B_{max} value is essentially equal to the 20 μM F-actin monomer concentration used in the reaction, indicating a 1:1 binding stoichiometry of headpiece/actin. These binding results for HP67 are in good agreement with previously determined binding constants and stoichiometry (*1*, *31*).

Replacement of tryptophan 64 by either alanine or tyrosine results in a nearly complete loss of specific binding (Figure 6). W64A has extremely weak binding and likely binds only nonspecifically. The conservative change to tyrosine in W64Y appears to retain some residual binding, but the K_D is well in excess of 100 μM. If we fit the W64Y data to eq 1, the fits are poor with large errors on the values of K_D, B_{max}, and NS. If we force the fitting by fixing the B_{max} and NS values to be the same as the wild type and R37A mutant and fit only the K_D, the best fit is with a K_D value of 151 μM. We take this to be an estimate of the lower boundary of the binding constant of this mutant. Thus, the tryptophan residue at position 64 is critical for F-actin recognition and binding by headpiece domains.

We also tested the role of the conserved positive charge at position 37 found in most headpiece sequences. In villin, position 37 is an arginine and is predicted to be one of the charged crown residues. We replaced this residue with alanine (R37A) and assayed F-actin binding using the sedimentation assay. Unlike the W64 mutants, the R37A data can be readily fit by eq 1, with a K_D of 24 ± 5.7 μM and B_{max} value of 23 ± 1.6 μM. The K_D is about 5-fold higher than the wild-type sequence, indicating that this charge contributes to F-actin affinity but is not essential for specific binding. Like HP67, the B_{max} value for R37A is essentially the same as the F-actin monomer concentration, indicating a specific 1:1 binding stoichiometry.

The crystal structures of the two actin-binding mutants, W64Y and R37A, are essentially identical to the wild-type structure except for the difference in their respective side-chain replacements. The mutants also retain the high thermostability of the wild-type sequence, with thermal unfolding midpoints in excess of 70 °C. Therefore, the loss of actin affinity by these mutants is not a consequence of changes in their structure or stability. The loss of the positively charged side chain in the R37A mutant likely reduces the F-actin affinity through loss of charge-neutralizing interactions with the highly negative surface of F-actin, which has net charge of −11 per monomer. For the W64Y mutant, there is only a small amount of hydrophobic surface lost and the overall shape and charge potential surface are nearly identical to the wild-type structure. This suggests that the tryptophan ring of W64 fits tightly into a pocket on the actin surface that is not satisfied by the smaller aromatic ring of tyrosine. The extra hydroxyl group on the tyrosine may also contribute unfavorable interactions.

In conclusion, the high-resolution crystal structure of HP67 coupled with those of the two mutants that replace residues involved in F-actin binding provide new insight into the function of villin-type headpiece domains. These structures provide the details of the packing of the core of villin headpiece that includes the thermostable 35-residue subdomain, with high precision. We also show that the conserved positive charge at position 37 contributes significantly to F-actin affinity but is not required for specific F-actin binding. In contrast, the invariant tryptophan at position 64 is essential for F-actin recognition because even conservative replacement with another aromatic residue (tyrosine) results in a dramatic decrease in binding.

ACKNOWLEDGMENT

We thank Dr. Wilson S. Colucci, Department of Medicine, Boston University School of Medicine, for providing densitometer facilities and the National Synchrotron Light Resource beamline X8C.

REFERENCES

1. Vardar, D., Chishti, A. H., Frank, B. S., Luna, E. J., Noegel, A. A., Oh, S. W., and McKnight, C. J. (2002) Villin-type headpiece domains show a wide range of F-actin-binding affinities, *Cell Motil. Cytoskeleton 52*, 9−21.
2. Glenney, J. R. J., Geisler, N., Kaulfus, P., and Weber, K. (1981) Demonstration of at least two different actin-binding sites in villin, a calcium-regulated modulator of F-actin organization, *J. Biol. Chem. 256*, 8156−8161.
3. Bretscher, A., and Weber, K. (1980) Villin is a major protein of the microvillus cytoskeleton which binds both G and F actin in a calcium-dependent manner, *Cell 20*, 839−847.
4. Pinson, K. I., Dunbar, L., Samuelson, L., and Gumucio, D. L. (1998) Targeted disruption of the mouse villin gene does not impair the morphogenesis of microvilli, *Dev. Dyn. 211*, 109−121.
5. Ferrary, E., Cohen-Tannoudji, M., Pehau-Arnaudet, G., Lapillonne, A., Athman, R., Ruiz, T., Boulouha, L., El Marjou, F., Doye, A., Fontaine, J. J., Antony, C., Babinet, C., Louvard, D., Jaisser, F., and Robine, S. (1999) *In vivo*, villin is required for Ca^{2+}-dependent F-actin disruption in intestinal brush borders, *J. Cell Biol. 146*, 819−830.
6. Kumar, N., Zhao, P., Tomar, A., Galea, C. A., and Khurana, S. (2004) Association of villin with phosphatidylinositol 4,5-bisphosphate regulates the actin cytoskeleton, *J. Biol. Chem. 279*, 3096−3110.
7. Vardar, D., Buckley, D., Frank, B., and McKnight, C. (1999) NMR structure of an F-actin binding "headpiece" motif from villin, *J. Mol. Biol. 249*, 1299−1310.
8. McKnight, C. J., Matsudaira, P. T., and Kim, P. S. (1997) NMR structure of the 35-residue villin headpiece subdomain, *Nat. Struct. Biol. 4*, 180−184.
9. Lee, M. R., Baker, D., and Kollman, P. A. (2001) 2.1 and 1.8 Å average C-α rmsd structure predictions on two small proteins, HP-36 and S15, *J. Am. Chem. Soc. 123*, 1040−1046.
10. Duan, Y., and Kollman, P. (1998) Pathways to a protein folding intermediate observed in a 1 μs simulation in aqueous solution, *Science 282*, 740−744.
11. Mukherjee, A., and Bagchi, B. (2003) Correlation between rate of folding, energy landscape, and topology in the folding of a model protein HP-36, *J. Chem. Phys. 118*, 4733−4747.
12. Fernandez, A., Shen, M. Y., Colubri, A., Sosnick, T. R., Berry, R. S., and Freed, K. F. (2003) Large-scale context in protein folding: Villin headpiece, *Biochemistry 42*, 664−671.
13. Islam, S. A., Karplus, M., and Weaver, D. L. (2002) Application of the diffusion-collision model to the folding of three-helix bundle proteins, *J. Mol. Biol. 318*, 199−215.
14. Zagrovic, B., Snow, C. D., Shirts, M. R., and Pande, V. S. (2002) Simulation of folding of a small α-helical protein in atomistic detail using worldwide-distributed computing, *J. Mol. Biol. 323*, 927−937.
15. Liu, Y. X., and Beveridge, D. L. (2002) Exploratory studies of *ab initio* protein structure prediction: Multiple copy simulated annealing, AMBER energy functions, and a generalized born/solvent accessibility solvation model, *Proteins: Struct., Funct., Genet. 46*, 128−146.
16. Sullivan, D. C., and Kuntz, I. D. (2002) Protein folding as biased conformational diffusion, *J. Phys. Chem. B 106*, 3255−3262.
17. Lin, C. Y., Hu, C. K., and Hansmann, U. H. E. (2003) Parallel tempering simulations of HP-36, *Proteins: Struct., Funct., Genet. 52*, 436−445.
18. Friederich, E., Vancompernolle, K., Huet, C., Goethals, M., Finidori, J., Vandekerckhove, J., and Louvard, D. (1992) An actin-binding site containing a conserved motif of charged amino acid residues is essential for the morphogenic effect of villin, *Cell 70*, 81−92.
19. Doering, D. S., and Matsudaira, P. T. (1996) Cysteine scanning mutagenesis at 40 of 76 positions in villin headpiece maps the F-actin binding site and structural features of the domain, *Biochemistry 35*, 12677−12685.
20. Rossenu, S., Leyman, S., Dewitte, D., Peelaers, D., Jonckheere, V., van Troys, M., Vandekerckhove, J., and Ampe, C. (2003) A phage display-based method for determination of relative affinities of mutants. Application of the actin-binding motifs in thymosin β 4 and the villin headpiece, *J. Biol. Chem. 278*, 16642−16650.
21. Vermeulen, W., Vanhaesebrouck, P., van Troys, M., Verschueren, M., Fant, F., Goethals, M., Ampe, C., Martins, J. C., and Borremans, F. A. M. (2004) Solution structures of the C-terminal headpiece subdomains of human villin and advillin, evaluation of headpiece F-actin-binding requirements, *Protein Sci. 13*, 1276−1287.
22. Frank, B. S., Vardar, D., Chishti, A. H., and McKnight, C. J. (2003) The NMR structure of dematin headpiece reveals a dynamic loop that is conformationally altered upon phosphorylation at a distal site, *J. Biol. Chem. 2*, 2.
23. Frank, B. S., Vardar, D., Buckley, D. A., and McKnight, C. J. (2002) The role of aromatic residues in the hydrophobic core of the villin headpiece subdomain, *Protein Sci. 11*, 680−687.
24. Pardee, J. D., and Spudich, J. A. (1982) Purification of muscle actin, *Methods Enzymol. 85*, 164−181.
25. Edelhoch, H. (1967) Spectroscopic determination of tryptophan and tyrosine in proteins, *Biochemistry 6*, 1948−1954.
26. Dauter, Z., and Dauter, M. (1999) Anomalous signal of solvent bromides used for phasing of lysozyme, *J. Mol. Biol. 289*, 93−101.
27. Terwilliger, T. C., and Berendzen, J. (1999) Automated MAD and MIR structure solution, *Acta Crystallogr., Sect. D: Biol. Crystallogr. 56*, 965−972.
28. Terwilliger, T. C. (2000) Maximum likelihood density modification, *Acta Crystallogr., Sect. D: Biol. Crystallogr. 56*, 965−972.
29. Jones, T., Zou, J., and Cowan, S. (1991) Improved methods of building protein models in electron density maps and the location of error in these models.
30. Brünger, A. T., Adams, P. D., Clore, G. M., DeLano, W. L., Gros, P., Grosse-Kunstleve, R. W., Jiang, J. S., Kuszewski, J., Nilges, M., Pannu, N. S., Read, R. J., Rice, L. M., Simonson, T., and Warren, G. L. (1998) Crystallography and NMR system: A new software suite for macromolecular structure determination, *Acta Crystallogr., Sect. D: Biol. Crystallogr. 54*, 905−921.
31. Pope, B., Way, M., Matsudaira, P. T., and Weeds, A. (1994) Characterization of the F-actin binding domains of villin: Classification of F-actin binding proteins in to two groups according to their binding sites on actin, *FEBS Lett. 338*, 58−62.
32. Schägger, H., and von Jagow, G. (1987) Tricine−sodium dodecyl sulfate−polyacrylamide gel electrophoresis for the separation of proteins in the range from 1 to 100 kDa, *Anal. Biochem. 166*, 368−379.
33. Sambrook, J., Fritsch, E. F., and Maniatis, T. (1989) *Molecular Cloning: A Laboratory Course*, 2nd ed., Cold Spring Harbor Press, Cold Spring Harbor, NY.
34. Swillens, S. (1995) Interpretation of binding curves obtained with high receptor concentrations−Practical aid for computer analysis, *Mol. Pharm. 47*, 1197−1203.
35. McKnight, C. J., Doering, D. S., Matsudaira, P. T., and Kim, P. S. (1996) A thermostable 35-residue subdomain within villin headpiece, *J. Mol. Biol. 260*, 126−134.
36. Wang, M., Tang, Y., Sato, S., Vugmeyster, L., McKnight, C. J., Raleigh, D. P., Trott, O., and Palmer, A. G., III (2003) Dynamic NMR line-shape analysis demonstrates that the villin headpiece subdomain folds on the microsecond time scale: Temperature-dependent dynamics of the villin headpiece helical subdomain, an unusually small thermostable protein, *J. Am. Chem. Soc. 125*, 6032−6033.
37. Kubelka, J., Eaton, W. A., and Hofrichter, J. (2003) Experimental tests of villin subdomain folding simulations, *J. Mol. Biol. 329*, 625−630.
38. Vugmeyster, L., Trott, O., McKnight, C. J., Raleigh, D. P., and Palmer, A. G., III (2002) Temperature-dependent dynamics of the villin headpiece helical subdomain, an unusually small thermostable protein, *J. Mol. Biol. 320*, 841−854.
39. Brewer, S. H., Tang, Y. F., Raleigh, D. P., Vu, D. M., Dyer, R. B., and Franzen, S. (2004) Infrared T-jump investigation of the folding kinetics of the villin headpiece subdomain, *Biophys. J. 86*, 497a−497a.

BI050850X